Proceedings of Global Power and Propulsion Society
ISSN-Nr: 2504-4400
GPPS Shanghai25
September 4-6, 2025
www.gpps.global

GPPS-TC-2025-248

EFFECTS OF INTAKE LENGTH ON FLUTTER STABILITY OF A FAN BLADE

Venkata Y.T. Chennuru*
School of Aeronautics and Space
Universidad Politécnica de Madrid
28040 Madrid, Spain
e-mail: ve.chennuru@upm.es

Fanzhou Zhao
Department of Mechanical Engineering
Imperial College London
London, UK
e-mail: fanzhou.zhao11@imperial.ac.uk

Roque Corral†
School of Aeronautics and Space
Universidad Politécnica de Madrid
28040 Madrid, Spain
e-mail: roque.corral@upm.es

Mehdi Vahdati
School of Aeronautics and Space
Universidad Politécnica de Madrid
28040 Madrid, Spain
e-mail: mehdi.vahdati@upm.es

ABSTRACT

Next-generation turbofan aero-engines are expected to feature larger fan diameters to reduce specific thrust and enhance overall efficiency. To counteract the associated weight and drag penalties, more compact nacelles with shorter intakes are being adopted. However, shortening the intake fundamentally alters the aeroacoustics, potentially changing the flutter stability of the fan blade. This paper investigates the impact of reducing the intake length on the flutter bite using a three-dimensional unsteady Computational Fluid Dynamics (CFD) model. The flutter characteristics of the fan blade are first analysed across three intake configurations: an infinitely long intake, a conventional intake (L/D = 0.5), and a short intake (L/D = 0.25) representative of Ultra-High Bypass Ratio (UHBR) engine designs. Results indicate that shortening the intake shifts the flutter bite from part-speed operation to design-speed conditions, creating a significant stability risk. The CFD findings are compared against analytical flutter index too, demonstrating strong agreement.

INTRODUCTION

Fan flutter is a self-induced aeroelastic instability that remains a critical problem in the design and operation of modern turbofan engines. This phenomenon is driven by the interaction between blade vibrations and unsteady aerodynamic forces, and can restrict the engine's operating range. Among the most challenging occurrences of flutter is the so-called 'flutter bite' that occurs before the stall boundary (Vahdati et al., 2015).

Fig. 1 illustrates a typical fan map showing the relationship between the fan pressure ratio as a function of inlet mass flow, including constant speed lines, stall and flutter boundaries, and the design working line. This plot indicates that flutter can significantly restrict the

*Corresponding author
†Professor of Aerospace Engineering, Department of Fluid Mechanics and Aerospace Propulsion, Universidad Politécnica de Madrid

This work is licensed under **Attribution-NonCommercial-NoDerivatives 4.0 International** (CC-BY-NC-ND).
See: https://creativecommons.org/licenses/by-nc-nd/4.0/legalcode

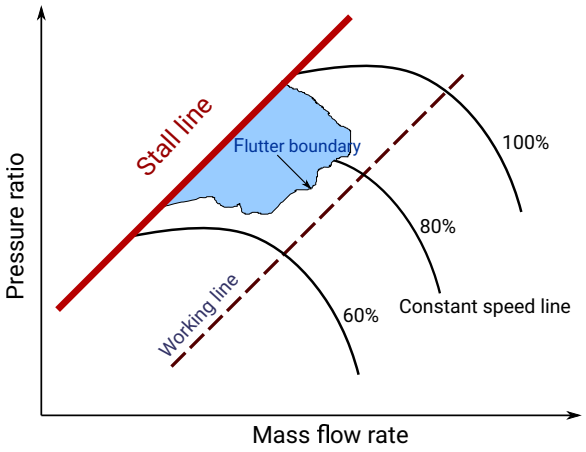

Figure 1: Sketch of typical fan map and flutter-bite boundary

stable operating region of the fan as flutter can occur at higher mass flows (closer to the design working line) than stall. This phenomenon occurs at part speed conditions in the first flap mode (1F) with low Nodal Diameters (2-3 NDs for the fan studied here), as extensively documented in previous research (Lee et al., 2017; Aotsuka and Murooka, 2014; Vahdati et al., 2015; Bontemps et al., 2021; Schnell and Frey, 2022). This acoustic flutter is linked to the acoustic coupling between the fan and the upstream intake duct (Zhao et al., 2017; Bontemps et al., 2021; Schnell and Frey, 2022).

In an aeroengine, the upstream running acoustic modes induced by the blade vibration are reflected at the intake highlight, reaching the fan blade at a different phase (Bontemps et al., 2021; Vahdati et al., 2015). Depending on the amplitude of the reflected wave, and the phase of the reflected acoustic wave with respect to the emitted wave, the effects could either be stabilising or destabilising the fan blade (Zhao et al., 2017). While the amplitude of the reflected wave depends on the parameters like axial Mach Number in the duct (M_x), frequency of vibration (ω), and intake diameter (D) (González-Monge et al., 2024; Zhao et al., 2017), it is independent of the length of the intake. However, the phase of the reflected wave highly depends on the intake length and determines the nature of the intake effect (stabilising or not). Therefore changing the intake length can mainly impact the region of flutter bite.

Over the past decade, several researchers have studied the phenomenon of flutter bite in aero-engines and its dependence on intake characteristics. Zhao et al. (Zhao et al., 2017) proposed a 1D analytical model capable of predicting the speed range over which fans become susceptible to flutter, with predictions within 2% of experimental measurements. Their work also showed that reducing the intake length from L/D=1.8 to 1, leads to a slower variation of the flutter index with a change in rotation speed and a reduction of the band intensity. Bontemps et al. (Bontemps et al., 2021) investigated flutter prediction mechanisms using CFD, an acoustic solver and an analytical model for an intake length of L/D = 2.5. Their results showed good agreement between the CFD and the acoustic solver predictions, while their analytical method struggled to accurately capture the phase of the reflected wave. More recently, Schnell and Frey (Schnell and Frey, 2022) employed the Harmonic Balance method to study the acoustic feedback mechanisms and found good agreement with the simple analytical model. These studies highlight the growing understanding of intake acoustic interactions.

Despite the known role of intake acoustics in fan blade flutter, the effect of varying intake length on flutter behaviour has not been extensively studied, especially in transonic fans of next-generation UHBR engines. To address this gap, the present study uses a three-dimensional unsteady CFD model to investigate the impact of intake length on fan blade aeroelastic stability. The intake configurations examined in this study—specifically, the L/D = 0.5 case representing conventional designs and the L/D = 0.25 case aligned with UHBR engines—highlight the practical relevance of this investigation. To isolate the effect of intake length, only the straight section of an axisymmetric cylindrical intake is varied, while the nose cone, intake lip, and other features are kept constant.

CFD provides a valuable and cost-effective alternative to complex and expensive real-world experiments for studying such aeroelastic phenomena. The primary objective of this paper is to understand the influence of intake length on the flutter stability of a fan blade during Sea-Level-Static (SLS) operation using CFD simulations. The CFD results are compared with the analytical tool developed by (González-Monge et al., 2024). To understand and explain how the intake length affects the aerodynamic damping of the fan, the flutter analysis is conducted in three stages:

1. **Effect of intake length on Fan Aerodynamics:** The first step compares the steady-state aerodynamics of the fan blade with an infinitely long intake (referred to as blade-only), short intake (L/D=0.25), and a long or conventional intake (L/D =0.5). Since the

short intake is very aggressive, the loading and the flow on the blade are carefully examined to match the other configurations.

   (a) **Baseline Flutter Stability:** Next, the flutter characteristics of the fan blade are assessed using the blade-only configuration. This reference case evaluates how key flow features—such as shock position, flow separation, and radial migration—influence aerodynamic damping. The damping computed from these simulations is referred to as 'blade only' damping in this paper.

2. **Effect of Intake Acoustics:** Finally, this step isolates the influence of intake reflection on blade flutter stability for both the intake geometries.

By systematically comparing the results from these stages, this study provides a detailed physical explanation of the change in acoustic flutter behaviour due to a change in the intake length using the acoustic theories and how it is ultimately affecting fan flutter stability. The findings offer critical insights for the aeroelastic design of future turbofan engines with compact nacelles.

TEST CASE AND NUMERICAL MODEL

Computational Model

The computational domain used in this study consists of three individual domains: the fan, the intake, and the downstream nozzle domain.

Fan Domain

The ACAT fan used in this work, developed by *AneCom AeroTest* (ACAT) (Blázquez-Navarro and Corral, 2023), is a transonic fan with a total pressure ratio of 1.42 and a tip Mach number of 0.9. It has 20 blades, a tip diameter of 865 mm, a hub-tip ratio of 0.33, and a tip gap of 0.2% of the span. This fan operates with a bypass stream containing 44 Outlet Guide Vanes (OGV) and a core flow with 44 Engine Sector Stator (ESS). Since the main objective of this paper is to study and understand the unsteady interaction between the fan and the intake, these downstream components (OGV and ESS) are replaced by a straight duct. The duct extends 6.5 times the intake lip diameter (D_l) downstream.

Intake Domain

The intake geometry is based on the AIAA intake made available by the PAW 05 workshop. This axisymmetric cylindrical intake is scaled to fit the ACAT fan blade, and the intake lip definition is modified to allow the flow to separate at lower crosswind speeds. After scaling, the intake has a lip diameter D_l of approximately 1.1 times the intake inner diameter (D) and an outer-to-inner diameter ratio of 1.25. The intake is positioned centrally along the back wall of this domain, equidistant from the farfield, as seen in Fig. 2a. Two different configurations are considered in this study, as shown in Fig. 2a. The first is the conventional intake (or referred to as the long intake) with the fan positioned at a length-to-diameter ratio (L/D) of 0.5, and the second is the short intake with a L/D of 0.25. All the mean flow and distortion measurements are performed at the Aerodynamic Interface Plane (AIP), located 0.65 chords upstream from the fan tip leading edge (LE).

Meshing

Fan Mesh

A single-passage structured grid was created for the fan blade with HO grid topology using Fidelity V2023.1, yielding approximately 400k nodes per passage, which was then converted to an unstructured mesh format for compatibility with the CFD solver. The fan grid consists of 54 radial layers (46 layers on the blade and 8 equidistant layers in the tip gap region) and 32 azimuthal layers, maintaining y+ values between 30 and 100. This value of y^+ is used based on previous experience using the SA model with wall functions (Moreno et al., 2020). For unsteady simulations, the single passage mesh is expanded to a full-annulus mesh with 8 million nodes.

Intake Mesh

The intake mesh comprises approximately 10.5 million nodes. An unstructured hexahedral grid was generated using Ansys ICEM 2023R2, maintaining surface y+ values between 30 and 100. The mesh sizing of the intake is determined from the previous work of the authors in unsteady intake crosswind simulations (Chennuru et al., 2024a,b). Intake mesh has a finer resolution in and around the intake lip. The intake domain has 640 azimuthal and 54 radial layers to align with the fan domain. This mesh distribution is matched perfectly among all the interfaces of the three domains to improve the accuracy of the unsteady simulations. In the intake farfield boundaries, the mesh has a constant expansion ratio of 1.1 to reduce the overall node count.

Mechanical Model

The structural analysis was conducted using the CalculiX FEM solver. The solid model was constrained at the fir-tree attachment, while the effect of disk flexibility was deemed negligible. The analysis was restricted to the first flap (1F) mode as the rig tests and

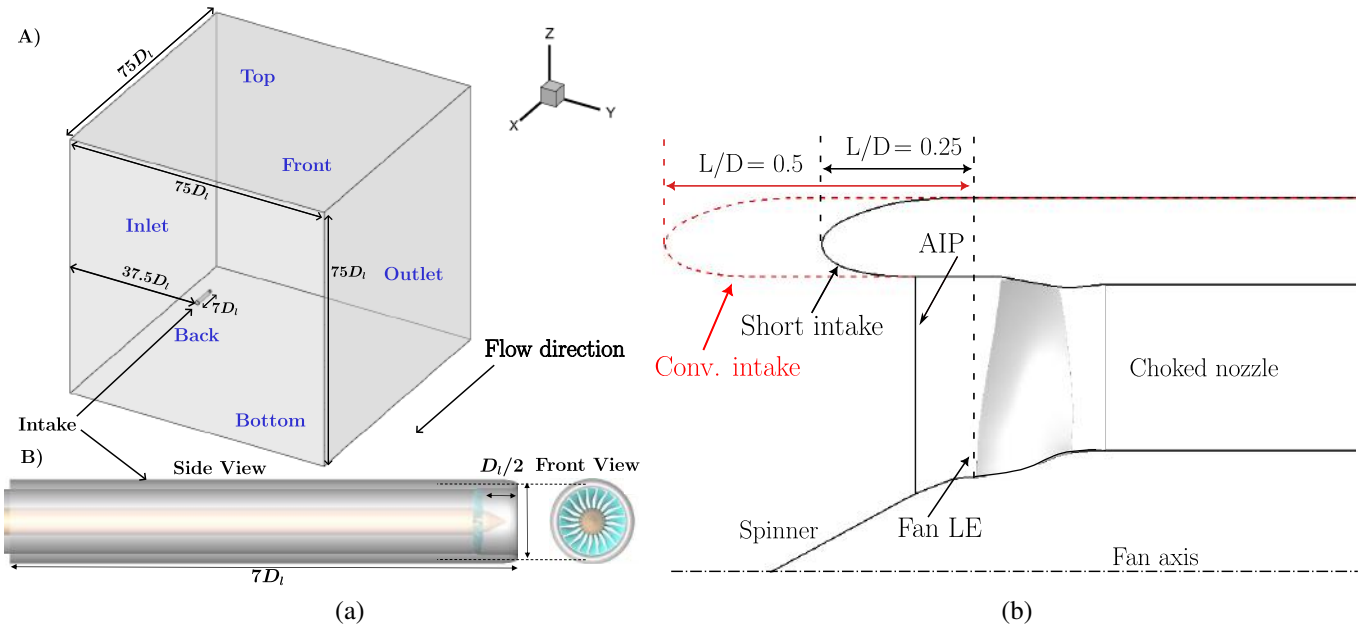

Figure 2: View of domain used in current computation; (a) Meridional view of the intake, fan and duct geometry, (b) Computational domain and boundaries.

numerical studies (Lee et al., 2017; Aotsuka and Murooka, 2014; Vahdati et al., 2015; Bontemps et al., 2021; Schnell and Frey, 2022) have shown that this type of flutter occurs in this mode at low nodal diameters (between 2 and 4 NDs). The structural mesh and the 1F mode shape are shown in Fig. 3. The natural frequency for the 1F mode is 1.6Ω at 90% shaft speed as shown in the Campbell diagram Fig. 3c, where Ω is the rotational speed. At the blade tip, the twist-to-plunge ratio for the 1F mode is 0.2 (Vahdati and Cumpsty, 2016).

For the aeroelastic computations, the modal displacement of the blade surface was interpolated onto the fluid domain mesh for one blade. The resulting mode shape was then expanded across all nodal diameters (NDs) of interest, as illustrated in Fig. 3b (for 2ND). The displacement of the boundary nodes is imposed following a prescribed motion (energy method). It is helpful to study the response of each mode to distortion and vibration in terms of modal force, which is given by

$$F = \int_{blade} \hat{\phi} \cdot p\hat{\mathbf{n}} dS$$

Where F is the modal force, p is the pressure on the blade surface, $\hat{\mathbf{n}}$ is the local unit normal, and $\hat{\phi}$ is the mass normalised mode shape (see Fig. 3).

Boundary Conditions

All the farfield inlet flow boundaries are set with Riemann invariant boundary conditions using the wind velocity vector and ambient pressure and temperature at Sea-Level-Static (SLS) conditions. The wind direction is at 0° angle to the intake as shown in Fig. 2a. The intake, spinner, blade, hub, and shroud are modelled as viscous walls using a wall function, while the farfield is considered as a flow boundary. The flow through the fan is controlled by placing a choked variable-area nozzle downstream of the fan. This nozzle allows the computation to be conducted at any point on the constant speed characteristic by modifying the nozzle area ratio. In steady computations, mixing planes are used at the intake/fan interface; sliding planes are used for full annulus unsteady simulations unless otherwise specified.

Numerical Solver

Numerical computations are carried out using the in-house CFD solver HADES, a 3D time-accurate, compressible, viscous, and finite-volume hybrid RANS / LES flow solver for unstructured grids. The flow variables are represented on the mesh nodes, and the numerical fluxes are calculated along the edges of the grid. The solver is based on the Spallart-Allmaras (SA) one-equation

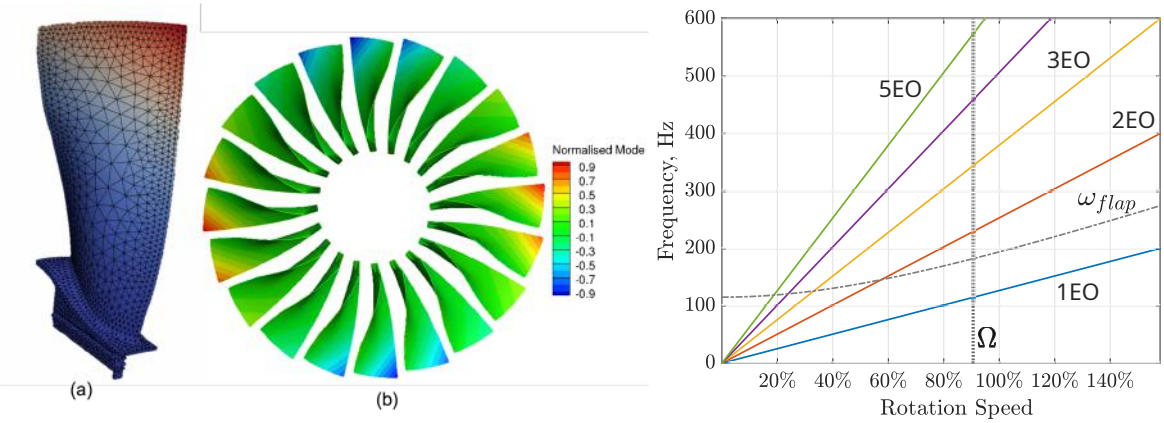

Figure 3: FE GRID AND 1F MODE (A), EXPANDED MODE SHAPE FOR 1F/2ND (B), CAMPBELL DIAGRAM (C)

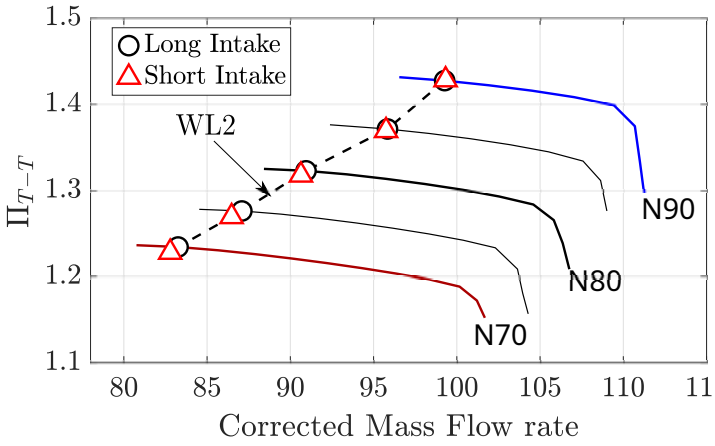

Figure 4: FAN MAP COMPARING THE OPERATING POINTS OF WL2 FOR LONG AND SHORT INTAKES.

turbulence model. The solution method is implicit and maintains second-order accuracy in space and time. Unsteady flow computations are performed using unsteady Reynolds-Averaged Navier-Stokes (URANS) equations. HADES was validated and verified in intake flow separation and ground vortex by Chennuru et al. (Chennuru et al., 2024b) and various 2D canonical flows and high-speed 3D compressible applications in previous publications by He et al. (He et al., 2022). Corral et al. (Corral et al., 2025) verified the prescribed motion and free-flutter analysis methods.

CFD strategy

Steady analysis

In the first step pseudo-steady results are obtained which are used as the initial condition for the unsteady computations. The domain used for steady state computations consists of a 360^o models of the intake but only single passage for the rotor and the nozzle. The interface boundary between different domains is modelled using mixing planes and the computations are performed using RANS. The total number of grid points for the steady analysis is 11 million. Although this type of modelling cannot model the transfer of circumferential non-uniformities between different blade rows, it can provide an approximation which can be used as an initial condition for the unsteady computations as the flow quantities such as mass flow will be matched between different domains.

Figure 4 presents the computed steady state fan performance between 70% to 90% corrected speed. At each fan speed, the characteristic curve is obtained by starting from a solution near the choked boundary and progressively closing the exit nozzle area until the stall boundary is reached. The stall boundary is defined as the last point along the constant speed characteristic where the slope

remains negative. Also, shown in this plot is the WL2 which is used later in this paper for flutter simulations. Additionally, the steady characteristics of the fan equipped with the short intake configuration along with WL2 are included for comparison with the long intake.

Unsteady flutter simulations

The domain used for unsteady flutter computations consists of a whole assembly model of all the rows (intake, fan and downstream nozzle). The interface boundaries between the blade rows are modelled as sliding planes. The steady single-passage solution is expanded to a full annulus and used to initialise the unsteady calculations.

Flutter computations are initiated by prescribing the motion of multiple NDs simultaneously within a single simulation, using a full annulus model of the fan (Corral et al., 2025). The amplitude of the prescribed motion for each ND is set at 0.25% of the blade chord at the tip. As demonstrated by Corral et al. (Corral et al., 2025), the prescribed vibration amplitude does not influence the computed aerodynamic damping. This approach remains valid if the interaction among different nodal diameters are weak, which is the case for tuned fan blades operating without distortion, where the aeroelastic modes coincide with the travelling waves of the different NDs.

There are 200 time steps in a vibration cycle for a 2ND mode in the stationary frame of reference. The simulations are performed until the aerodynamic forcing for all the NDs converges to a periodic state. Then, the periodic solution is postprocessed to extract the work-per-cycle associated with different nodal diameters. Further details regarding the flutter modelling methodology employed in this study can be found in (Corral et al., 2025).

Analytical Tool for Identifying the Intake Effects

It has been shown (Vahdati and Cumpsty, 2016) that a necessary condition for fan flutter is that the downstream acoustic field of the blades must be cut-off, while the upstream wave remains cut-on. Consequently, in the present study, the primary focus is placed on the upstream propagating acoustic wave generated at the fan's leading edge and its reflections from the intake highlight (the intake opening).

An analytical model is employed to assess the susceptibility of fans to flutter induced by acoustic reflections from the intake(González-Monge et al., 2024). This model predicts the propagation and reflection of acoustic waves within the intake duct based on established linear acoustic theories (Moinier and Giles, 2005), which assume perfectly rigid duct walls and negligible radial flow variations. A dimensionless parameter known as the flutter index β, is introduced to quantify the effect of intake reflections on fan aeroelastic stability. The flutter index is defined as $\beta = |a^+| \sin(\Delta\phi)$, where a^+ is the amplitude of the first radial mode returning to the fan face (the only cut-on flutter mode), and $\Delta\phi = \phi^- - \phi^+$ is the phase difference between the wave emitted by the fan and the returning one, respectively.

In this framework, a phase lag $\Delta\phi$ of -90^o corresponds to the most destabilising contribution. In contrast, a $\Delta\phi$ of $+90^o$ corresponds to the most stabilising effect. Accordingly, the positive (negative) values of the flutter index $\beta > 0$ ($\beta < 0$) are interpreted as a stable (unstable) contribution from the intake to fan flutter. It has been demonstrated that the computed flutter index aligns well with numerical predictions of aerodamping due to intake reflections (Zhao et al., 2017; González-Monge et al., 2024).

RESULTS AND DISCUSSIONS

To conduct this study, it was first necessary to define a speed range and select an appropriate operating line, as the computational cost of 3D nonlinear CFD limits the feasibility of analysing a large number of operating points. The chosen speed range and operating line were based on acoustic theory and prior experience, as detailed in Ref. (Chennuru et al., 2025). The operating line WL2 (Fig. 4) was selected so that the blade may flutter. Along the operating line WL2, the shocks were expelled at all speeds. The speed range was determined using the flutter index model based on Ref. (González-Monge et al., 2024), which considers the blade's first bending (1F) vibration frequency (f_{vib}), nodal diameter (m), fan rotational speed (Ω), intake Mach number (M), and the length (L), and the diameter of the intake duct (D).

As previously discussed, the aerodynamic damping of a fan blade results from the combined effects of blade-alone damping and damping introduced by the intake acoustics. To isolate and better understand the aerodamping characteristics associated with both short and long intake configurations, it is essential to study the blade-alone and intake damping effects separately. Therefore, the analysis begins with the blade-alone characteristics, which are directly related to the steady-state loading and the flow on the suction side of the blade.

Steady State Comparison Across Intake Configurations

The aerodynamic loading and flow characteristics on the fan blade are intrinsically linked to upstream flow properties, such as Mach number (M), static pressure (p), and swirl angle (α). Fig. 5 presents a comparison of the circumferentially averaged radial profiles for three intake configurations at 90% rotational speed along operating line WL2.

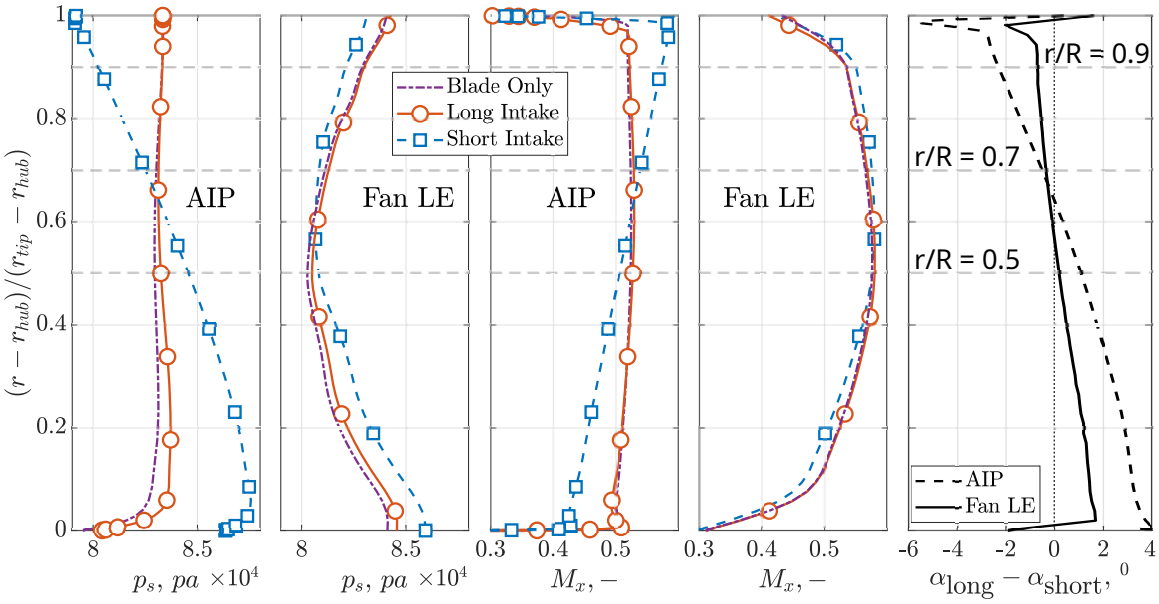

Figure 5: Comparison of circumferentially averaged radial profiles of Axial Mach Number, static pressure and difference in relative swirl angle at the AIP and the Fan LE for different intake configurations at 90% speed on WL2.

The comparison of the axial Mach number profile at the AIP reveals that both the blade-only and long intake configurations exhibit nearly uniform distributions. In contrast, the short intake configuration shows a noticeable increase in Mach number from hub to shroud. Similarly, static pressure profiles at the AIP exhibit a similar trend: while blade-only and long intake configurations maintain uniform pressure, the short intake demonstrates a pressure drop from hub to shroud.

These discrepancies suggest that in the short intake configuration, the intake lacks sufficient length for flow development, preventing it from becoming uniform before reaching the AIP. This results in a notable difference of approximately 2^oin the relative swirl angle (α) between the short and long intake configurations at 90% span on the AIP.

However, at the fan leading edge (LE, see Fig. 2b), located approximately 0.65 blade chords downstream of the AIP, the radial profiles converge. The flow in the short intake becomes more aligned with that in the long intake and blade-only configurations. This is evident from the radial distributions of both static pressure and axial Mach number, where the differences between the different intake configurations become minimal. At a span of 90% radius ($r/R = 0.9$), the difference in relative swirl angle between the short and long intake is reduced to just 0.5^o.

Figure 6a presents a comparison of the steady state blade loading at three radial spans (r/R=0.5, 0.7, and 0.9) at operating point A. Near the midspan locations (r/R=0.5 and 0.7), the differences in blade loading across the three intake configurations are negligible, consistent with the corresponding relative swirl angle profiles. However, at r/R=0.9, minor variations in shock position are observed between configurations. These discrepancies are attributed to the slight differences in relative swirl angle at this radial location.

Figure 6b displays the static pressure contours on the suction surface of the blade, superimposed with the streamlines, for both the short and long intake configurations at operating point A. A strong shock is present near the leading edge, followed by radial migration of the flow beginning around 65% span which is driven by a radial pressure gradient along the blade surface. Overall, the flow features in both cases appear nearly identical.

Based on these observations, it can be concluded that the blade-alone aerodynamic changes are negligible between long and short intake configurations.

Flutter Characteristics with Different Intake Configurations

Figure 7a shows the variation of the critical damping ratio for the 2ND mode with rotational speed along the operating line WL2, for the blade-only, long intake, and short intake configurations. Also shown in the figure is the difference in damping, ($\Delta\xi_{\text{aero}} = \xi - \xi_{\text{BO}}$), representing the additional aerodynamic damping introduced by intake reflections (intake damping) for both intake configurations.

It is first observed that the blade-only damping decreases with increasing rotational speed; this is due to the increased blade loading

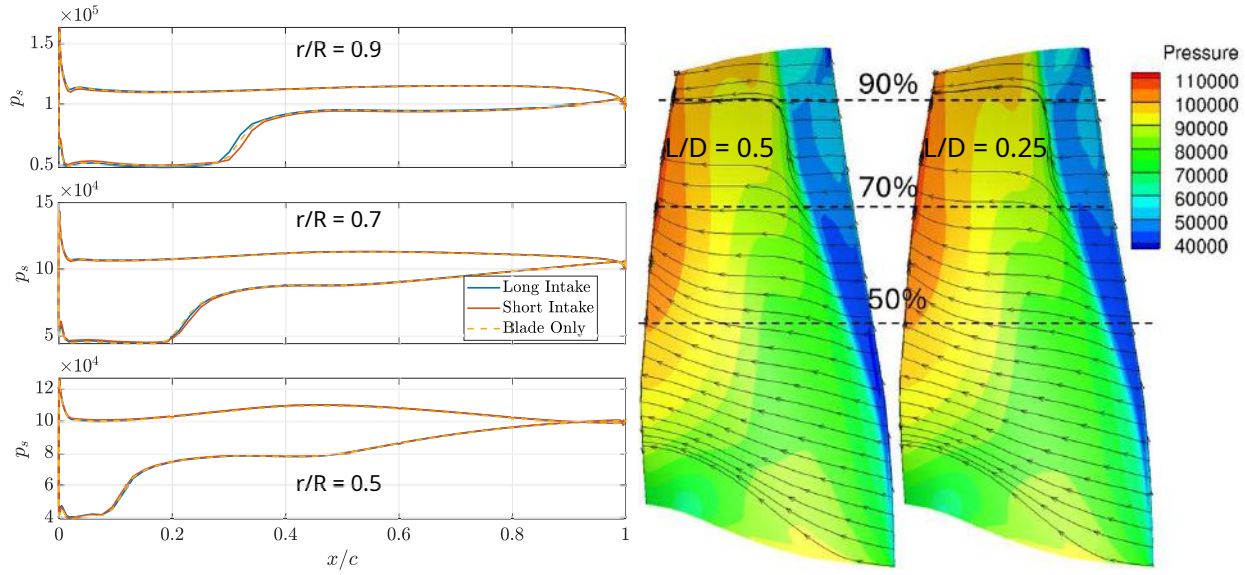

(a) Blade loading at different radial span

(b) Pressure on blade suction surface

Figure 6: Comparison of steady state blade loading among the three intake configurations at different radial spans (a), and flow on the suction surface of the blade for long and short intakes (b) at operating point A.

(Corral and Vega, 2017). For the long intake configuration, the damping is initially higher than the blade-only case at 70% speed. However, it decreases sharply, becoming negative between 78% and 83% speed, before increasing again and surpassing the blade-only damping at 90% speed. The intake aerodamping, $\Delta\xi_{aero}$, indicates destabilising effects in the 73%–87% speed range. Combined with the low blade-only damping in this interval, the fan blade became aerodynamically unstable between 78%-83% speeds—defining the flutter bite region for the long intake configuration.

The short intake configuration (L/D=0.25) maintains positive critical damping values at lower rotation speeds up to 85%. Beyond this point, the damping becomes negative, implying instability at the design speed. Therefore, for the short intake, the flutter bite shifts toward higher speeds, moving the instability region away from the low speed operation and into the design-speed range. The corresponding $\Delta\xi_{\text{aero}}$ confirms that the short intake configuration contributes to blade destabilisation at rotation speeds exceeding 83%.

For the vibration frequency (f_{vib}), fan's shaft speed (Ω), nodal diameter (m), intake Mach number (M), intake length (L) and diameter (D), a flutter index map is created for the ACAT fan. This map, shown in Fig. 7b for both the long and short intake configurations. with the operating points along WL2 superimposed for reference. The flutter index is plotted as a function of intake Mach number and blade vibration frequency in the stationary frame of reference, defined as $\omega = f_{\text{vib}} + m \times \Omega$.

In these flutter index plots, green regions represent stabilising (beneficial) contributions from the intake, red regions indicate the destabilising effects, and white regions denote neutral zones where the intake has little or no influence on flutter stability. Notably, the white region in the lower left corner—corresponding to low values of M and ω—represents the acoustic cut-off region, where the intake has a negligible impact on damping. For additional details, the reader is referred to the Refs. (Zhao et al., 2017; González-Monge et al., 2024).

Figure 7b shows strong agreement between the analytical prediction of intake effects and the CFD results for long and short intake configurations. For the long intake, the intake damping ($\Delta\xi_{\text{aero}}$) is negative between 77% and 82% rotational speed, closely matching the analytical prediction. The significant destabilising effect occurs at approximately 78% speed.

In contrast, the flutter index behaviour for the short intake is notably different. Overall, the regions exhibiting both stabilising and destabilising effects are much bigger. The cut-off region remains unchanged, as it is a function of M and ω alone and is not influenced by intake characteristics such as length, radius, or lip thickness.

Following the cut-off region, the intake begins to provide a stabilising effect. This region extends from 72% in the long intake case up to 81% in the short intake configuration. As a consequence, the subsequent destabilising region shifts to higher rotational speeds. This shift results in the fan blade becoming unstable at speeds above 82%, effectively moving the flutter bite closer to the design speed in the case of the short intake for 2ND mode.

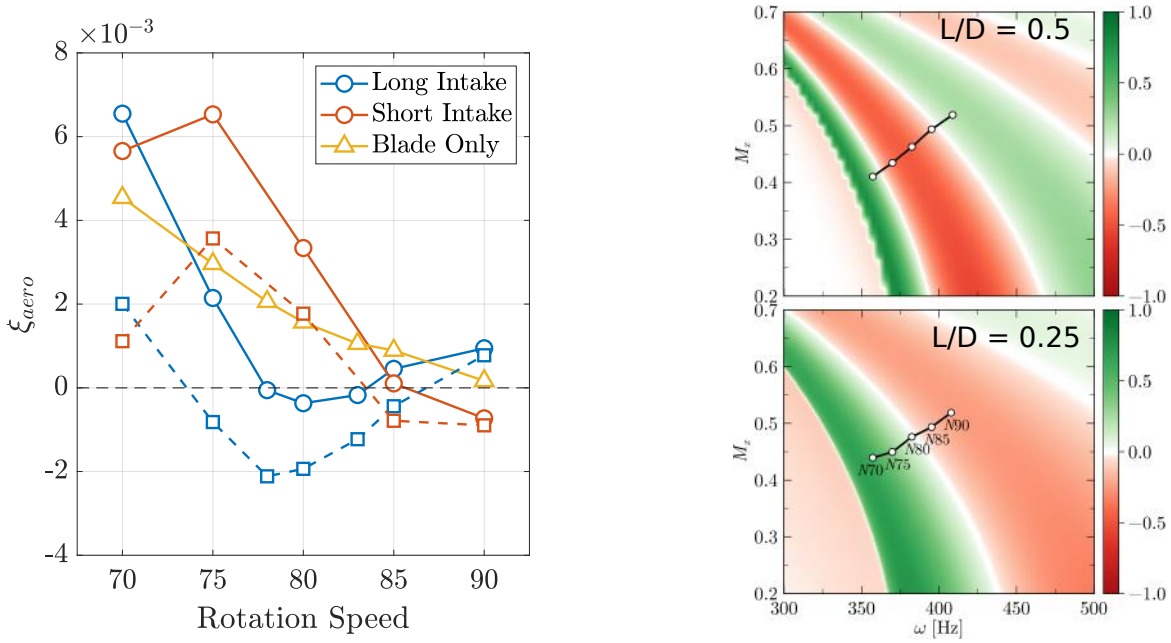

(a) Critical damping ratio vs speed

(b) Flutter index for long (top), short (bottom) intakes

Figure 7: Change in critical damping ratio vs speed for three different intake configurations on WL2 for 2ND mode.

Figure 8a illustrates the variation in critical damping ratio for 3ND mode with rotation speed along WL2, for the blade-only, long intake, and short intake configurations. Intake damping, $\Delta\xi_{\text{aero}}$, is also plotted for both intake configurations. Similar to the 2ND mode, the critical damping ratio for the blade-only case generally decreases with increasing speed. However, a notable exception occurs between 70% and 75% speed, where the damping increases. This behaviour is attributed to the transition of acoustic waves from cut-off to cut-on conditions, as discussed by (Vahdati and Cumpsty, 2016) and evident is in Fig. 8b. Furthermore, for both intake configurations, intake damping remains negligible up to 75% speed, since the acoustic waves are cut-off at these values of M_x and ω.

The long intake configuration exhibits negative $\Delta\xi_{\text{aero}}$ between 81% and 88% speed, based on the CFD computations. This observation agrees well with the predictions from the analytical tool. However, due to the higher blade-only damping for the 3ND mode compared to the 2ND mode, the overall aerodynamic damping, ξ_{aero}, remains positive across the entire speed range.

A similar trend is observed for the short intake configuration. While the CFD results confirm a shift in the destabilising region to higher speeds, as predicted by the analytical model, the total damping ξ_{aero} remains positive throughout. Consequently, the fan blade is aerodynamically stable in the 3ND mode across all operating speeds considered.

Figure 9 summarises these findings by illustrating the intake damping, expressed as $\Delta\xi_{\text{aero}}$ and β, plotted against rotational speed for both 2ND and 3ND modes with short and long intake configurations. Overall, the variation of intake damping obtained from CFD shows good agreement with the analytical predictions. In particular, the flutter bite identified in the 2ND mode for both intake configurations is well captured. These results demonstrate that the analytical flutter index tool provides a reliable and computationally efficient means to predict the onset of flutter and assess the impact of intake induced acoustic damping, thereby supporting intake design decisions for future engine architectures.

CONCLUSIONS

In this paper the influence of intake length on the intake acoustics and the aeroelastic stability of a transonic fan blade was studied. Using a high-fidelity 3D unsteady CFD solver, the flutter characteristics were evaluated for three intake configurations: an infinitely long intake to study the blade-alone damping, the conventional (or the long) intake with L/D=0.5, and a short intake with L/D=0.25 to study the intake effects. To isolate the effect of intake length and to ensure a clean comparison, the intake geometry was modified by shortening only the straight section of the duct, while keeping the nose cone, lip shape, and other geometric features identical in both the configurations. The analyses were performed on a working line near the stall boundary across a range of rotational speeds.

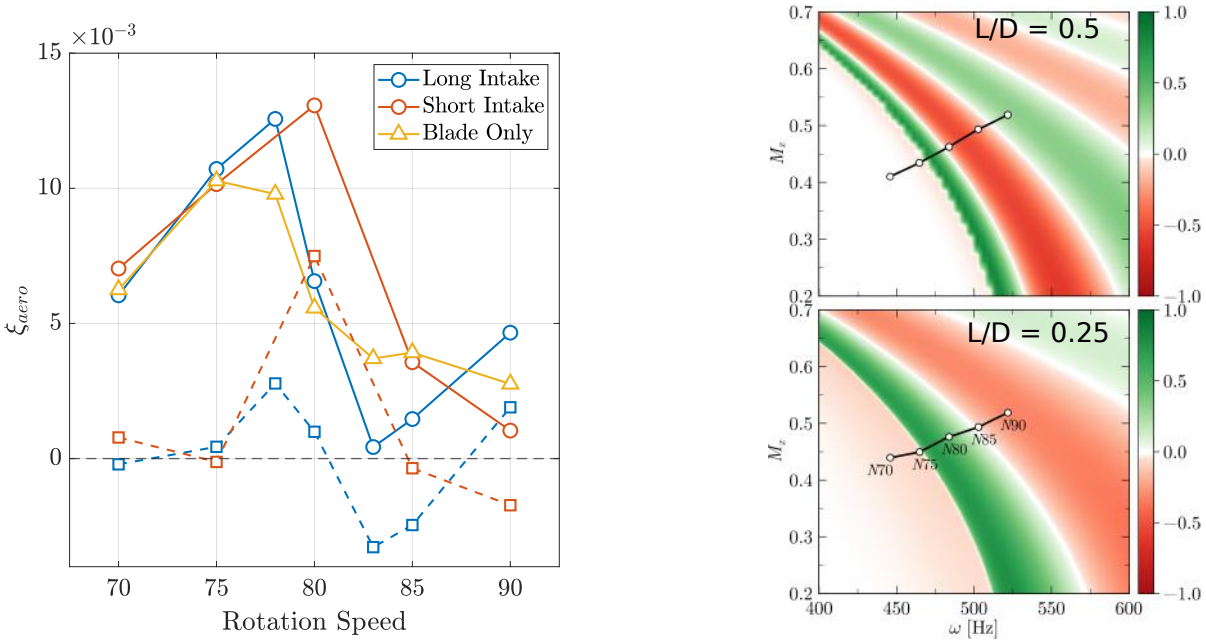

(a) Critical damping ratio vs speed

(b) Flutter index for long (top), short (bottom) intakes

Figure 8: Change in critical damping ratio vs speed for three different intake configurations on WL2 for 3ND mode.

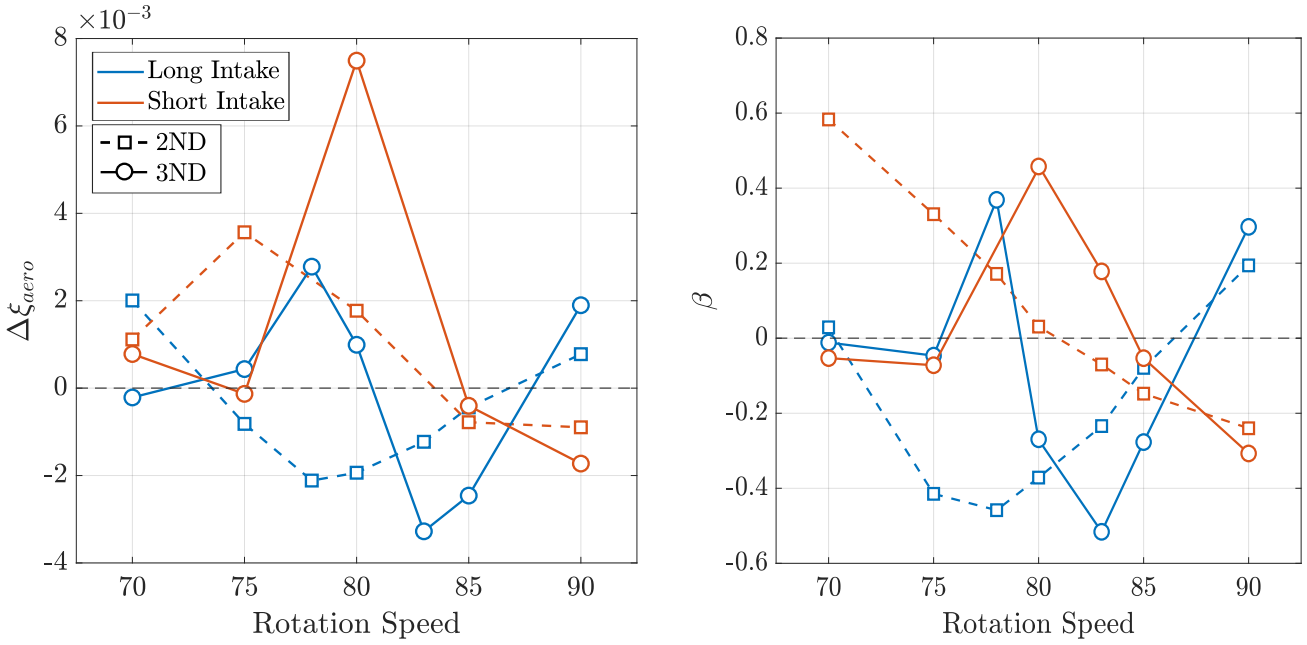

(a) Intake damping vs speed

(b) Flutter index vs speed

Figure 9: Comparison of intake damping computed using CFD (a) and using flutter index (b) for long and short intake with 2ND and 3ND.

The main conclusions of this work are:

1. **Change in Flutter Bite with Intake Length**: The results demonstrate that reducing the intake length has a big effect on the flutter stability. For the short intake configuration, it is observed that the flutter bite shifts from the part speed operation to higher speeds, including the design speed range. This poses a potential risk to the stability of the fan blade under realistic fan operating conditions.
2. **Validation of Analytical Flutter Index Tool**: The CFD results showed strong agreement with the analytical flutter index tool, displaying the predictive capability of the tool. The index maps effectively identified cut-off and cut-on acoustic regions and offered a quick insight into the stabilising and destabilising zones across various intake configurations.
3. **Design Implications for Future Turbofans**: As the next generation aero-engines aim to feature more compact nacelles with large diameters, the findings of this paper highlight the importance of accounting the intake effects. Engine designers must ensure that shortening the intake does inadvertently change the flutter bite into critical operating regions, especially around the design speed.

It should be noted that the present study employs an axisymmetric cylindrical intake model for the flutter analysis. While this simplified configuration enables consistent comparisons across different cases, real engine nacelle geometries are considerably more complex and may alter the intake acoustics. Further investigation is therefore required using more realistic intake models to examine if these effects are important. Additionally, the analysis focused on the extreme positions of the spinner nose cone; future work should explore more moderate spinner configurations.

ACKNOWLEDGEMENTS

The work is funded by Safran Aircraft Engines through the F^{2}EDORA-II research project with Universidad Politécnica de Madrid.

NOMENCLATURE

EO	Engine Order
c	chord
ND	Nodal Diameter
W	Work done
q	modal displacement
m	Modal mass
M	Mach number
D_l	Lip Diameter
H	Ground clearance
U	Velocity

Greek letters

ω	Vibration angular frequency (rad/s)
ξ_{aero}	Aero-damping ratio (%)
Ω	Shaft speed (%)
θ	Azimuthal coordinate

Sub-scripts

∞	Ambient conditions
i	intake duct
l	Lip of the intake duct

References

Aotsuka, M., Murooka, T., 2014. Numerical analysis of fan transonic stall flutter, in: Turbo Expo: Power for Land, Sea, and Air, American Society of Mechanical Engineers. p. V07BT35A020.

Blázquez-Navarro, R., Corral, R., 2023. Validation of broadband noise prediction methodology based on linearized navier-stokes analyses. Journal of Turbomachinery 145, 091002. doi:10.1115/1.4062398.

Bontemps, T., Aubert, S., de Pret, M., 2021. Prediction of the acoustic reflection in a realistic aeroengine intake with three numerical methods to analyze fan flutter. Journal of Turbomachinery 143, 101016.

Chennuru, V.Y.T., Corral, R., RodrÃguez-Blanco, S., Vahdati, M., Zhao, F., 2024a. Fan Non-Synchronous Forced Vibration Under Crosswind. Journal of Turbomachinery 147. doi:10.1115/1.4066915.

Chennuru, V.Y.T., Rodríguez-Blanco, S., Zhao, F., Corral, R., Vahdati, M., 2025. Fan flutter at mild wind conditions at sea-level-static, in: ASME Paper GT2025-153338, American Society of Mechanical Engineers.

Chennuru, V.Y.T., Zhao, F., Vahdati, M., 2024b. An optimal numerical strategy for intake in crosswind conditions. Journal of Engineering for Gas Turbines and Power 146, 071005. doi:10.1115/1.4064149.

Corral, R., Blanco-Rodriguez, S., Chennuru, V.Y., Zhao, F., Vahdati, M., 2025. A new non-linear time-domain flutter analysis approach for distorted flows. ASME Journal of Turbomachinery 147, 071014. doi:10.1115/1.4066915.

Corral, R., Vega, A., 2017. Quantification of the influence of unsteady aerodynamic loading on the damping characteristics of oscillating airfoils at low reduced frequency. Part I: Theoretical support. Journal of Turbomachinery 139, 0310009. doi:10.1115/1.4034976.

González-Monge, J., Pérez, J.M., Corral, R., Zhao, F., Vahdati, M., 2024. Conceptual analysis on the impact of acoustic liners in fan flutter. Journal of Turbomachinery 147, 041001. doi:10.1115/1.4066740.

He, X., Zhao, F., Vahdati, M., 2022. Detached Eddy Simulation: Recent Development and Application to Compressor Tip Leakage Flow, p. 011009. doi:10.1115/1.4052019.

Lee, K.B., Wilson, M., Vahdati, M., 2017. Numerical study on aeroelastic instability for a low-speed fan. Journal of Turbomachinery 139, 071004.

Moinier, P., Giles, M.B., 2005. Eigenmode Analysis for Turbomachinery Applications. Journal of Propulsion and Power 21, 973–978. doi:10.2514/1.11000. publisher: American Institute of Aeronautics and Astronautics.

Moreno, J., Dodds, J., Stapelfeldt, S., Vahdati, M., 2020. Deficiencies in the spallart-allmars turbulence model for the prediction of the stability boundary in highly loaded compressors. Journal of Turbomachinery 142, 121012. doi:10.1115/1.4047784.

Schnell, R., Frey, C., 2022. Acoustic feedback and its impact on fan flutter in short aeroengine intakes. Journal of Propulsion and Power 38, 631–646.

Vahdati, M., Cumpsty, N., 2016. Aeroelastic instability in transonic fans. journal of Engineering for Gas Turbines and Power 138, 022604.

Vahdati, M., Smith, N., Zhao, F., 2015. Influence of intake on fan blade flutter. Journal of Turbomachinery 137, 081002. doi:10.1115/1.4029240.

Zhao, F., Smith, N., Vahdati, M., 2017. A simple model for identifying the flutter bite of fan blades. Journal of Turbomachinery 139, 071003.